

Project Title:

**Theoretical study of interaction between tunneling electrons
and individual molecules at surfaces**

Name:

○Yusoo Kim, Kuniyuki Miwa, Emi Minamitani, Jaehoon Jung, Hiroshi Imada, Emiko Kazuma, Kan Ueji, Miyabi Imai, Ju-Hyung Kim

Laboratory at RIKEN:

Surface and Interface Science Laboratory

1. Background and purpose of the project,
relationship of the project with other projects

During the past decade, computer simulations based on a quantum mechanics have developed an increasingly important impact on solid-state physics and chemistry as well as on materials science. In field of material science, the surface chemistry is fundamentally important in many areas, such as molecular electronics, heterogeneous catalyst, fuel cell, etc. The adsorption of molecules onto a surface is a necessary prerequisite to any surface mediated chemical process. Understanding the bonding nature between the molecule and the surface on the basis of the electronic structure is therefore one of the most important issues in this field. The computational methods like density functional theory (DFT) have played a prominent role to elucidate the interaction between the molecule and the surface. In addition, the computational method can be useful to study the details of energy transport and conversion among photon and electrons mediated with adsorbate at solid surfaces in the nanoscale regime.

From the theoretical investigation of the adsorbed molecule on surface in combination with scanning tunneling microscopy and spectroscopy (STM/STS) experiment, we could expect the following research goals; 1) the deep understanding of the chemical/physical properties of an adsorbate on the surface not only in ground state but also in excited state, 2) the fine control of the chemistry on the surface. The overall purpose of our theoretical work

is closely related with research goal - describing the details of energy transport and conversion at solid surfaces and interfaces in the nanoscale regime - of our laboratory, Surface and Interface Science laboratory.

2. Specific usage status of the system and calculation method

We have been studying the molecular adsorption on the well-defined metal surface using computational method in combination with experimental method. In our studies, first-principles simulations have been carried out using the Vienna Ab-initio Simulation Package (VASP) code and Quantum Espresso code in the density functional level of theory. The pure DFT methods have been mostly used and the inner electrons are replaced by projector augmented wave pseudopotentials (PAW). The climbing image nudged elastic band method (CI-NEB) is used to determine the transition states that are confirmed by imaginary frequency modes. In most of cases, STM image simulations are performed using Tersoff-Hamann approach. The computational results are compared with the available experimental result obtained from STM in our group. For the gas phase molecules, the Gaussian09 program with atomic-orbital basis set is also effectively utilized to obtain stable geometries and corresponding electronic structures.

We also have been studying the many-body phenomena in molecular adsorption system, in particular the Kondo effect. The characteristic electronic state resulting from the Kondo effect, so-called Kondo singlet state appears as a sharp peak structure (Kondo peak) at the Fermi level (E_F) in STS. In order to simulate the Kondo peak, we build numerical renormalization group (NRG) code and the STS simulation code based on the Keldysh Green's function method.

3. Result

(1) STM simulation of NH on Pt(111) [*ACS Nano*, **9**, 8303 (2015)].

The interaction of hydrogen with metal surfaces has been studied for decades and is still of great interest for its role in hydrogenation reactions, hydrogen storage, and fuel cells. Hydrogen atoms on metal surfaces are difficult to detect by many surface science techniques because hydrogen is such a poor electron scatterer. In the present study, we characterized the atomic structure of H and NH on a N-covered Pt surface using STM experiment in combination with DFT calculations.

We found that hydrogen atoms appear as protrusions on a N-covered Pt(111) surface, making them readily observable even at very low coverages. Figure 1a shows the honeycomb structure of the $p(2 \times 2)$ -N phase on Pt(111). In this structure, Pt atoms that are not adjacent to N atoms are visible in the STM images and form a (2×2) -Pt lattice and are referred to as Pt-visible, whereas Pt atoms that are bonded to N atoms are referred to as Pt-invisible because they are not resolved. Such a (2×2) -Pt lattice serves as a well-ordered template for H adsorption. After exposing the N-covered surface to $H_2(g)$ at 50 K, H atoms are seen as protrusions (Figures 1b and 1c) and are separated by two Pt lattice constants from

each other. White circles superimposed on the images in Figure 1a–c indicate the Pt where the H atoms can adsorb. The presence of N shifts the most stable binding site for H from a hollow to an atop site. Figure 1d shows the model corresponding to Figure 1c, where Pt-visible is colored purple and Pt-invisible gray. The H and N atoms are shown as red and blue, respectively. The $p(2 \times 2)$ -N/Pt(111) surface thus serves as an ideal system for manipulating individual H atoms.

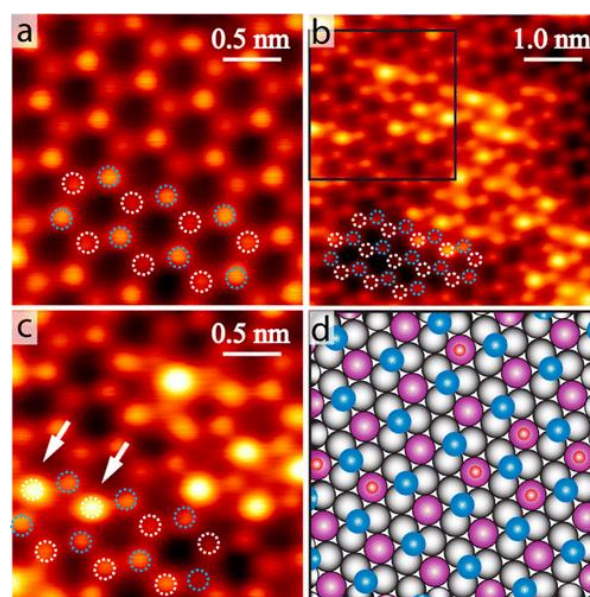


Figure 1. (a) Honeycomb structure of $p(2 \times 2)$ -N ($2.5 \text{ nm} \times 2.5 \text{ nm}$, $V_s = 5 \text{ mV}$, $I_t = 1 \text{ nA}$). (b) Hydrogen atoms adsorbed on $p(2 \times 2)$ -N ($5 \text{ nm} \times 5 \text{ nm}$, $V_s = 5 \text{ mV}$, $I_t = 1 \text{ nA}$). (c) Zoomed-in image of the black square in (b) ($2.5 \text{ nm} \times 2.5 \text{ nm}$, $V_s = 5 \text{ mV}$, $I_t = 1 \text{ nA}$). White arrows indicate H atoms. (a–c) Blue and white circles indicate N and Pt atoms, respectively. (d) Model showing H atoms adsorbed on $p(2 \times 2)$ -N corresponding to (c). Gray, Pt-invisible; purple, Pt-visible; blue, N atom; red, H atom.

Annealing the surface with adsorbed hydrogen to 300 K leads to the formation of NH, which is characterized by a triangular shape, as indicated by the blue arrow in Figure 2. The triangular-shaped NH molecules occupy fcc hollow sites, as do the N atoms. The triangular shape of the molecule can be understood as the perturbation of the electronic properties of the nearest Pt atoms by the NH.

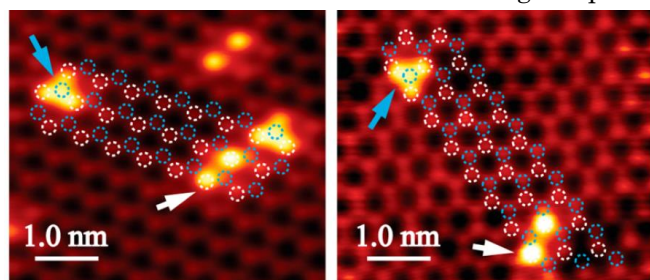


Figure 2. STM images of NH and H on $p(2 \times 2)$ -N/Pt(111). Blue and white arrows indicate an NH molecule and a H atom, respectively.

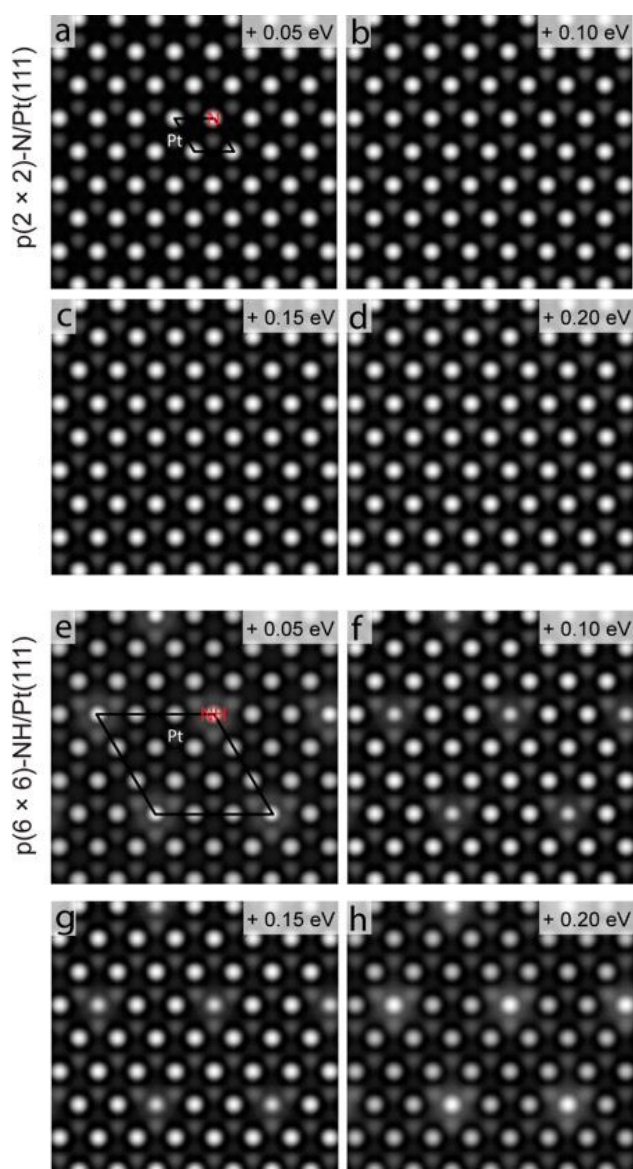


Figure 3. (a–d) Simulated STM images with an iso-surface level of 0.05 e/bohr^3 of $p(2 \times 2)$ -N/Pt(111) for the indicated bias voltages. (e–h) Simulated STM images of $p(6 \times 6)$ -NH/Pt(111). Unit cells and the positions of Pt, N, and NH are indicated in (a) and (e).

In Figure 3, we show simulated STM images for $p(2$

$\times 2)$ -N/Pt(111) obtained from DFT calculations using the Vienna ab initio simulation package (VASP), in which ion–electron interactions are described by projector-augmented wave (PAW) pseudopotentials and the exchange–correlation is described by the Perdew–Burke–Ernzerhof (PBE) approximation. The Pt(111) surface was modeled with a (6×6) supercell of six layers with the bottom two layers fixed and the other four layers relaxed. Only the fcc hollow site was considered for nitrogen adsorption. The surface irreducible Brillouin zone was sampled with $4 \times 4 \times 1$ Γ -centered grids. The cutoff energy of the plane wave expansion was 400 eV. The Tersoff–Hamann scheme was used to simulate the STM images from DFT calculations. As shown in the top panel of Figure 3, no specific bias dependence was observed for $p(2 \times 2)$ -N/Pt(111) from 0.05 to 0.20 eV. The honeycomb structure in the simulated STM images agrees well with the experimental results (Figure 1a). The simulated appearance of isolated NH molecules for an assumed $p(6 \times 6)$ -NH layer are shown in Figure 3e–h. The triangular shape of an NH molecule agrees well with the experimental results.

(2) Elucidation of isomerization pathways of a single azobenzene derivative using an STM [*J. Phys. Chem. Lett.*, **6**, 4239 (2015)].

Azobenzene is one of the most attractive molecules for molecular switches, which operate based on the difference in the molecular structure and the electric conductance between its cis and trans isomers. Although the cis–trans isomerization in azobenzene has been intensively studied with the primary focus on photochromism, the predominant isomerization pathway is still a controversial issue. In this study, owing to the proper design of the functional groups, i.e., structural probes, into azobenzene molecule, the isomerization pathways of the azobenzene derivative (IMA) were clearly distinct with STM experiment, as schematically shown in Figure 4.

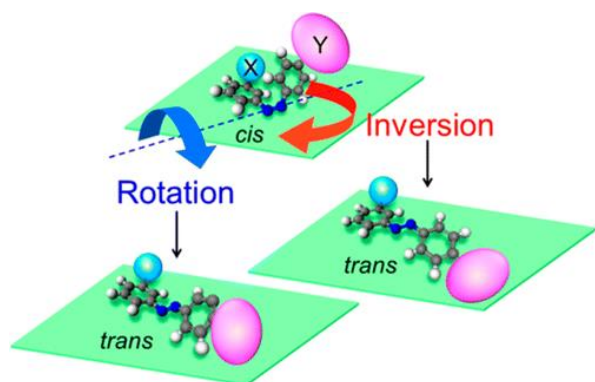


Figure 4. Two isomerization pathways for an IMA molecule on a metal surface: inversion and rotation.

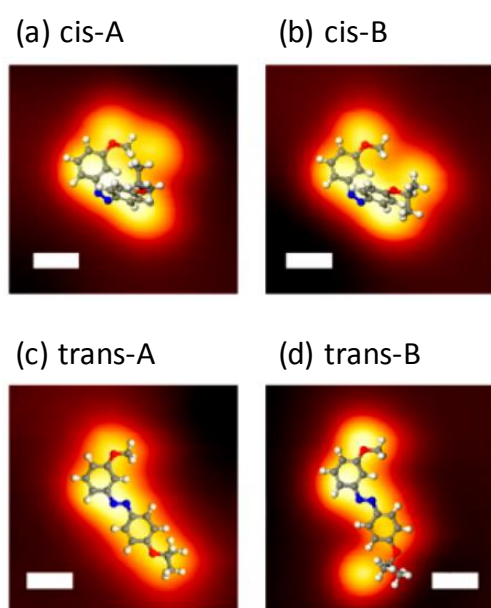


Figure 5. STM images of four different IMA isomers superimposed with the ball-and-stick models optimized in the gas phase.

Before the adsorption, similar to azobenzene, the IMA molecules were initially in the trans conformation, which is thermodynamically most stable in the gas phase. The Ag(111) surface was exposed to the IMA molecules at as low as <50 K to investigate the cis–trans isomerization of individual isolated molecules. The STM images show two types of adsorbates; each molecule showed a bright ellipsoidal and two small spherical protrusions, corresponding to the azobenzene backbone and two different alkoxy groups, respectively. The molecules with two different shapes initially present on the as-adsorbed surface were assigned as two types of

cis-isomers (cis-A and B), as shown by the ball-and-stick models (Figures 5a and 5b), based on several local minima optimized by gas-phase density functional theory (DFT) calculations. The injection of tunneling electrons at 1.5 V induces apparent change in the shape of the target cis-molecules; two additional molecular shapes were observed. The elongated molecules resulting from electron injection into cis-isomers were assigned as the trans-isomers (trans-A and B) based on several local minima optimized by gas-phase DFT calculations (Figures 5c and 5d).

Further STM experiments in combination with DFT calculations revealed that the potential energy surfaces for the isomerization between cis- and trans-IMA were schematically constructed based on the reaction probability as a function of the applied sample bias voltage for the corresponding reactions. Our observations are summarized as (1) cis-IMA is thermodynamically more favorable than trans-IMA on the surface, (2) isomerization pathways between cis- and trans-IMA molecules can be clearly distinguished, (3) both the inversion and rotation pathways are available for isomerization on a metal surface, strongly depending on the adsorption structures of the molecule, and (4) isomerization reactions from cis- to trans-IMA and from trans- to cis-IMA occur through electronic and vibrational excitations, respectively.

(3) Seamless growth of a supramolecular carpet [*Nat. Commun.*, **7**, 10653 (2016)]

Organic thin films (OTFs) have received much attention for their potential in various electronic and optoelectronic device applications, since they have outstanding advantages (that is, low cost, low weight and mechanical flexibility) in comparison with standard inorganic technologies. In particular, it has been recognized in recent years that organic/metal

(O/M) interfaces at which charge carriers are injected into OTFs play a crucial role in the operation and performance of organic devices. Various interactions at the O/M interface, such as surface–molecule and intermolecular interactions, are of great importance in the formation of intermolecular networks and organic epitaxy, and have a strong correlation with their electronic structures. Although the purity and uniformity of OTFs at the O/M interfaces have profound effects on the operating characteristics of organic devices, the formation of OTFs with high interfacial uniformity on metal surfaces has suffered from the intrinsic limitation of molecular ordering imposed by surface step edges, due to the relatively weak intermolecular interactions between organic molecules. Extensive research efforts in the development of OTFs with high interfacial uniformity on metal surfaces have mostly focused on examining the formation of covalent bonding and supramolecular complexes between organic precursors via laborious post-treatments, such as epitaxial surface polymerization and metal–organic coordination. However, the creation of widely uniform OTFs on metal surfaces that maintain structural integrity based on non-bonding intermolecular interactions remains a challenge for further development and enhancement of organic devices fabricated by one-step deposition of organic molecules.

In this study, we successfully demonstrate the formation of a supramolecular carpet (SMC), with a widely uniform interfacial structure and high adaptability, on a metal surface, via a one-step deposition process. The geometric and electronic structures of the SMC were investigated by means of scanning tunneling microscopy/spectroscopy (STM/STS) and density functional theory (DFT) calculations. For this work, BTDA-TCNQ molecule (bis[1,2,5]thiadiazolotetracyanoquinodimethane) was used as the key building block with which to realize the SMCs, not only on a single crystal gold

(Au) surface but also on a pre-annealed amorphous Au surface. The rhombic structure of BTDA-TCNQ exhibits twofold symmetry with two mirror planes, allowing perpendicular alignment of two electrostatically opposite symmetry axes consisting of electronegative and electropositive end groups, respectively. It, therefore, enables equivalent intermolecular interactions along the four sides of the molecule. Such rhombic structure also facilitates access of neighboring molecules to each other via high electrostatic interactions in the four directions, which leads to topographically favorable intermolecular interactions as shown in Figure 6.

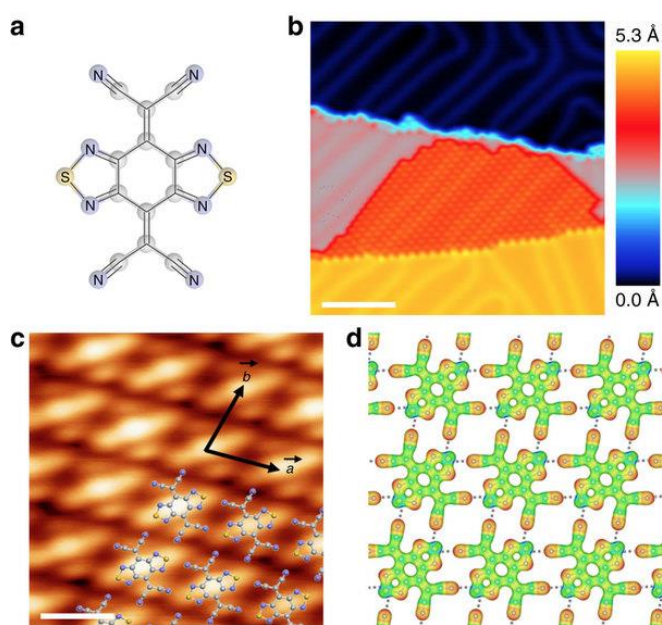


Figure 6. (a) The chemical structure of BTDA-TCNQ. (b) STM image of BTDA-TCNQ/Au(111), which shows that the molecular network of BTDA-TCNQ grows from the step edge at the lower terrace ($V_s = 1.0$ V, $I_t = 1.0$ nA, scale bar = 10.0 nm). (c) Close-up STM image of the network structure formed by BTDA-TCNQ ($V_s = 2.0$ V, $I_t = 1.0$ nA, scale bar = 1.0 nm). (d) The electrostatic potential map of the DFT-optimized BTDA-TCNQ network. Blue to red corresponds to positive to negative charges.

On deposition of BTDA-TCNQ on the Au(111) surface, decoration at the step edge occurs first, and then growth of a highly ordered SMC proceeds from the step edge across the lower terrace without further

nucleation occurring on the terrace (see Figures 6a and 6b). This step-flow growth mode of the SMC exhibits a quasi-epitaxial nature with an in-plane azimuthal orientation of BTDA-TCNQ. The reconstructed herringbone structures of Au(111) beneath the SMC are readily observed in the STM images, which reveals that the adsorption of BTDA-TCNQ on the Au(111) terraces does not involve quenching of the Au(111) Shockley surface state. These experimental observations indicate that the surface–molecule interfacial interactions of BTDA-TCNQ/Au(111) are sufficiently weak so that lateral diffusion of the molecules across the Au(111) terraces is possible. Contrary to the weak adsorption characteristics of BTDA-TCNQ/Au(111), the partial positive and negative charges of the S and N atoms of BTDA-TCNQ, respectively, introduce effective attractive interactions (that is, the S–N intermolecular interactions) between the neighboring molecules, which determine the array of the molecules in the SMC, as shown in Figures 1c and 1d. Detailed analysis of the STM images gave lattice constants for the SMC unit cell of $a=b=10.0\pm 1.0$ Å and $\gamma=80\pm 5^\circ$, which are noticeably similar to those achieved by the S–N intermolecular interactions of the coplanar molecular network in the single crystal structure of BTDA-TCNQ. DFT calculations were also performed to examine the formation of SMC and to confirm its stability in terms of intermolecular interactions. On the basis of the experimental observations of weak surface–molecule interactions, the substrate was not considered in the calculations. For comparisons among a variety of initial geometries, various molecular orientations rotated by 10° increments were considered with the experimentally observed periodicity of the intermolecular network structure. On the basis of our computational approach, three non-equivalent local potential minima were found corresponding to the varied molecular orientations (see Figure 7).

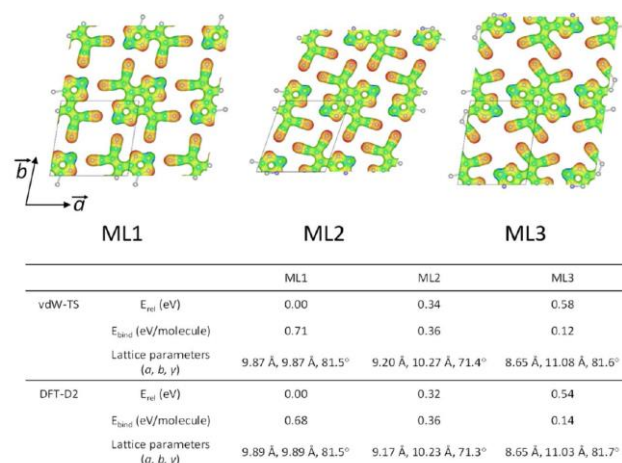


Figure 7. Electrostatic potential maps of BTDA-TCNQ molecular layers corresponding to various molecular orientations. Relative energies, binding energies, and optimized lattice parameters are presented in bottom table, which were calculated using two different functionals, vdW-TS and DFT-D2.

The experimentally observed azimuthal orientation is most favorable with the highest binding energy per molecule of ~ 0.70 eV (see Figure 1d), which is more stable than the other two local potential minima by >0.30 eV. Note that the calculated binding energy of ~ 0.70 eV per molecule is highly competitive with the dipole polarization energy arising from donor–acceptor complexation in the charge-transfer crystal. The higher stability of the geometric structure of the SMC, in comparison with the followed second and third local potential minima, mainly originates from the relative orientations of electronegative cyano ($-\text{CN}$) groups between the neighboring molecules. The electrostatic repulsions between the $-\text{CN}$ groups are easily expected in both second and third local potential minima rather than the S–N intermolecular interactions (see Figure 7), which implies that the S–N intermolecular interactions are an impetus for the formation of SMC. The calculated lattice constants of the SMC unit cell ($a=b=9.9$ Å and $\gamma=81.5^\circ$) are almost identical to our STM observations, and the calculated distance for the S–N contacts (~ 2.80 Å) is also well matched with that of the crystal structure of BTDA-TCNQ (~ 3.04 Å).

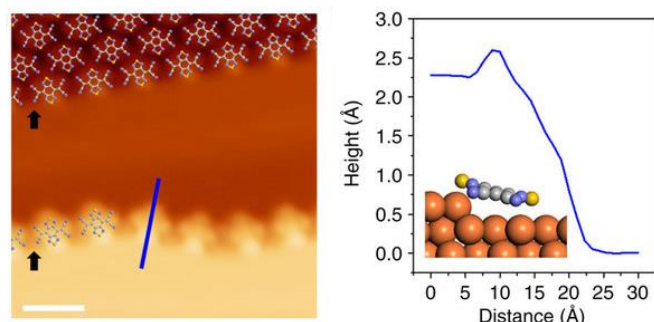


Figure 8. STM image of the BTDA-TCNQ molecules which lean down from the upper terrace to the lower terrace at the step edge ($V_s = 0.5$ V, $I_t = 0.5$ nA, scale bar = 2.0 nm). The height profile along the blue line in e. corresponding to the slanting adsorption structure of BTDA-TCNQ at the step edge is presented here.

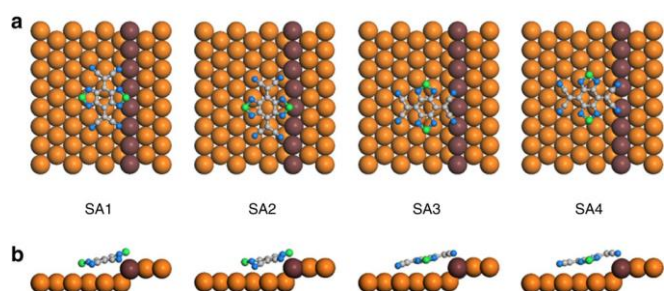


Figure 9. (a,b) Optimized geometries of four different hypothetical model structures of BTDA-TCNQ adsorbed at the step edge of Au(111) (designated ‘SA1’, ‘SA2’, ‘SA3’ and ‘SA4’, respectively) by DFT calculations. The S–S molecular axes of the molecules are perpendicular to the step line in ‘SA1’ and ‘SA2’, and parallel in ‘SA3’ and ‘SA4’. Side views of a are shown in b.

Table 1 | Relative energies, adsorption energies and optimized nearest atomic distances of S···Au and –CN···Au of four adsorption models, ‘SA1’, ‘SA2’, ‘SA3’ and ‘SA4’.

	SA1	SA2	SA3	SA4
E_{rel} (eV)	0.00	0.17	0.52	0.53
E_{ads} (eV)	2.64	2.47	2.12	2.11
<i>Step edge</i>				
S···Au (Å)	3.12 (× 2)	2.54		
–CN···Au (Å)	2.18	2.56	2.31	2.34
<i>Terrace</i>				
S···Au (Å)	3.34	3.33	3.61	3.69
–CN···Au (Å)	3.17	2.36	2.68	3.14

The optimized distances at the step edge and on the terrace are presented, respectively. In ‘SA1’, a bidentate fashion of S···Au at the step edge is denoted with ‘× 2’.

The strong non-bonding intermolecular interactions, balanced with surface–molecule interfacial interactions and site-specific rearrangements, i.e., slanting adsorption (SA), of the BTDA-TCNQ molecules near surface step edges, enable the step-flow growth mode for the SMC formation (see Figure 8). This can lead to an extension of the SMC over step edges of the Au surface without loss of its structural integrity, and results in a covering with high interfacial uniformity over multiple surface steps and terraces, even on the pre-annealed amorphous Au surface prepared on a glass substrate. To gain deeper insight into the SA structure of BTDA-TCNQ at the step edges, DFT calculations were performed in consideration of four different adsorption models (designated ‘SA1’, ‘SA2’, ‘SA3’ and ‘SA4’, respectively) as shown in Figure 9 and Table 1. Among these structure models, the most stable adsorption structure of the BTDA-TCNQ molecule at the step edge was found to be ‘SA1’ with the adsorption energy of 2.64 eV. In ‘SA1’, the S–S molecular axis of BTDA-TCNQ is perpendicular to the step line, and the two S atoms are located on the upper and lower terraces, respectively. Compared with ‘SA3’ that is the most stable adsorption structure with the S–S molecular axis parallel to the step line, ‘SA1’ shows higher adsorption energy by 0.52 eV, which is consistent with the experimental observations of the SA structure at the step edges. The detailed geometric interpretation of the computational results indicates that the –CN groups of the BTDA-TCNQ molecule significantly contribute to determination of the adsorption structure at the step edges. Side views of the molecular adsorption structures clearly reveal that the –CN groups are displaced from the molecular plane and become closer to the surface, compared with the S atoms (see Figure 3b). In the most stable ‘SA1’, the nearest atomic distance between the molecule and the reactive Au atoms of the step edge (–CN···Au_{edge}) is 2.18 Å, and is much shorter than the S···Au_{edge} distance of 3.12 Å even though the S atom of

BTDA-TCNQ is interacting with the two Au_{edge} atoms. The higher stability of ‘SA1’ than ‘SA3’ also can be deduced from the shorter $-\text{CN}\cdots\text{Au}_{\text{edge}}$ distance in ‘SA1’ than that of ‘SA3’ by 0.13 Å. Combined with the $-\text{CN}\cdots\text{Au}_{\text{edge}}$ interactions, the relatively weak $\text{S}\cdots\text{Au}_{\text{edge}}$ interactions in ‘SA1’ also possibly participate in determining the adsorption structure when no existing $\text{S}\cdots\text{Au}_{\text{edge}}$ interaction in ‘SA3’ is considered. In addition, the charge density difference map of the most stable ‘SA1’ structure clearly reveals the partial charge transfer from the surface to the molecule through the $-\text{CN}$ groups at the step edge (see Figure 10), and the corresponding amount of the partial charge transfer evaluated by Bader population analysis is 0.68e. The computationally estimated feature of the partial charge transfer strongly supports the surface–molecule interfacial interactions localized at the step edges, resulting from the step dipole as will be discussed in relation to the STS spectra.

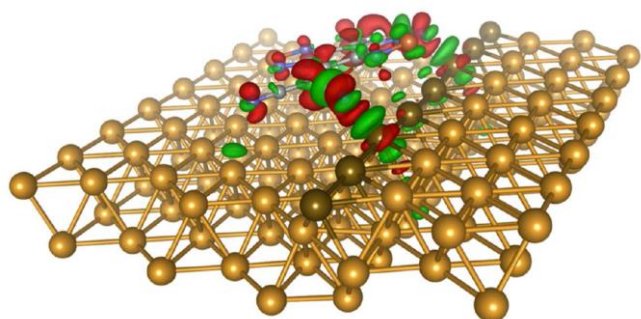


Figure 10. Charge density difference map for “SA1”. The charge density difference map of the BTDA-TCNQ molecule adsorbed at the step edge of Au(111), “SA1”. Red and green regions correspond to electron-gain and -depletion regions, respectively (iso-value = ± 0.002 e/bohr³).

(4) Spatially extended underscreened Kondo state from collective molecular spin [*Phys. Rev. B*, **92**, 075144 (2015)]

Understanding the molecular magnetism is a key issue in the realization of molecular spintronics and

the design of novel organic magnetic materials. Contacting molecules with electrode, which is a prerequisite for device application, drastically changes the molecular magnetism. One fundamental cause is the Kondo effect which screens the molecular spin by conduction electrons and forms the Kondo resonance state at the Fermi level. In molecular Kondo systems, the contribution from the molecular ligands give rise to rich physical phenomena, which would pave a way to control and tailor the molecular magnetism. It has been reported that the vibration and charge transfer in the molecular ligand influences the shape and spatial distribution of the Kondo resonance. Another example is the ligand symmetry driven orbital-spin coupled Kondo effect.

In this study, we show that the Mn phthalocyanine (MnPc) molecule on Pb(111) is a new example in which the strong coupling between the metal center and the molecular ligand induces a unique type Kondo effect. In this system, the interplay between the Kondo effect and the exotic electronic states

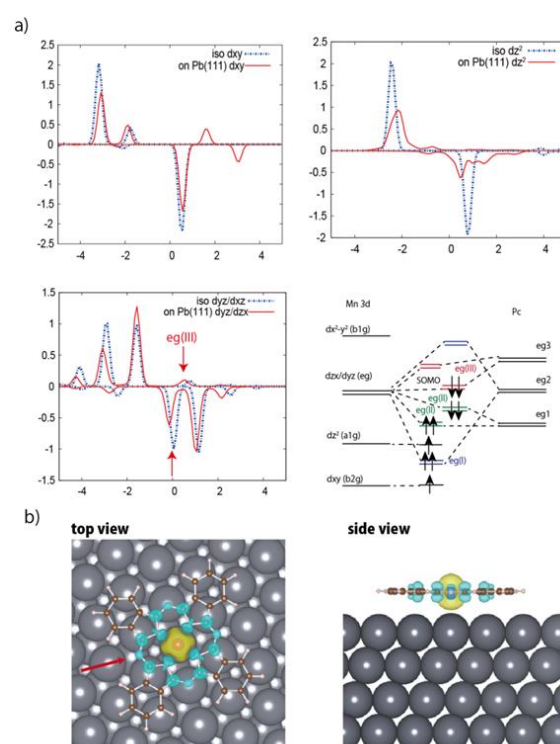


Figure 11. a) projected DOS in MnPc/Pb(111) b) top view and side view of spin spatial distribution

(superconductivity and quantum well state) in the Pb substrate has been discussed in the previous studies. However, the mechanism of the Kondo effect itself is still controversial. Up to now, three different models are proposed: 1) Kondo screening of $S=1/2$ at Mn dxy, 2) two-stage Kondo screening of $S=1$ state from Mn dzx/dyz (d π) and dxy orbital, 3) underscreened Kondo effect from $S=3/2$ to $S=1/2$ state occurs at Mn dz2 and d π orbitals.

In the present study, we investigated this system both experimentally and theoretically in order to clarify the mechanism of the Kondo effect. First, the low temperature scanning tunneling spectroscopy (STS) observations show that the distribution of the Kondo resonance is rather than limited at the Mn atom center, but uniformly extends over the pyrrole ring in the Pc ligand: none of the above three models can explain these results.

To gain insight into the origin of the spectroscopic features, DFT calculations were performed. On Pb(111), the calculation results for several different adsorption configurations show that MnPc preferentially adsorbs at the on-top site. The obtained aligned direction of MnPc and Pb (111) lattice determined in DFT calculation is consistent with experimental results. The adsorption considerably changes the MnPc magnetic state. The total magnetic moment decreases from 3.0 μ_B to 2.1 μ_B , which is approximately interpreted as the total spin changing from $S=3/2$ to $S=1$. The resulting $S=1$ magnetic state is explained by the strong d- π interaction between the Mn d π orbital and the ligand π -orbitals and occupation changes in the Mn dxy, dz2 and d π orbitals (Fig. 11(a)). The dxy orbital PDOS has nearly no change after adsorption, reflecting a weak interaction with Pb(111) due to its distribution plane parallel to the substrate. On the contrary, the peak structure of the dz2 orbital PDOS becomes much broader after adsorption, indicating a strong hybridization with the substrate. The spin

polarization of dz2 orbital is reduced but still kept after adsorption. The reduction of spin polarization is due to an increase in the occupation of the ligand state. In the d π orbital PDOS, peaks corresponding to the ligand state shift to a low-energy side after adsorption, i.e., the occupation in this state increases. The ligand orbital antiferromagnetically couples to the d π orbital which ferromagnetically couples to the other Mn d-orbitals. Thus, the injected electron has a minority spin, decreasing the total magnetic moment of the molecule. The summation of the spatial distribution of the majority spin at Mn center and the minority spin at ligand part matches the spatial distribution of the Kondo resonance (Fig. 11(b)).

Then, we construct the model Hamiltonian to explain the Kondo effect based on this ab-initio calculation results. In the model Hamiltonian, we considered that the Pb substrate hybridized only with Mn dz2 orbitals. Furthermore, we ignored the two-fold degeneracy in the ligand and the d π states. Since these orbitals are approximately half-filled and not directly hybridized with the substrate, reduction of the orbital degeneracy does not alter the total spin and the universality class of the Kondo model. The resulting model Hamiltonian becomes an extended Kondo model, which includes one conduction channel, 4 localized spins, and the magnetic interactions between them.

$$H = \sum_{k\sigma} \varepsilon_{k\sigma} c_{k\sigma}^\dagger c_{k\sigma} + \sum_{kk'\sigma\sigma'} J c_{k\sigma}^\dagger(\sigma) c_{k'\sigma'} c_{k'\sigma'} \cdot S_0 + J_H \sum_{\substack{\mu,\mu'=0 \\ \mu \neq \mu'}}^2 S_\mu \cdot S_{\mu'} + J_{AF} S_1 \cdot S_3 \quad (1)$$

where $\mu=0,1,2,3$ correspond to the localized spins of Mn dz2, d π state, Mn dxy, and ligand state, respectively. $c_{k\sigma}^\dagger$ ($c_{k\sigma}$) is the fermion creation (annihilation) operator for the conduction electron with spin σ . J is the s-d interaction and σ is the Pauli matrix. J_H is the FM Hund's coupling and J_{AF} is the AFM interaction between the d π and ligand state.

The precise values of J , J_H , and J_{AF} are unknown. Only, the order of $J_H \sim 1.0\text{eV}$ can be estimated from DFT calculation data. If $J_H > J_{AF} \gg T_K$, as the temperature decreases, the spin in MnPc is first locked into the $S=1$ state due to the large J_H and J_{AF} . The Kondo effect then occurs on this collective $S=1$ spin state at much lower temperatures, which can rationalize the observed spatial extension of the Kondo resonance. The numerical renormalization group simulation based on the above model well reproduces the experimental results.

(5) Electronic and magnetic effects of a stacking fault in cobalt nanoscale islands on the Ag (111) surface [*Phys. Rev. B*, **92**, 064421 (2015)]

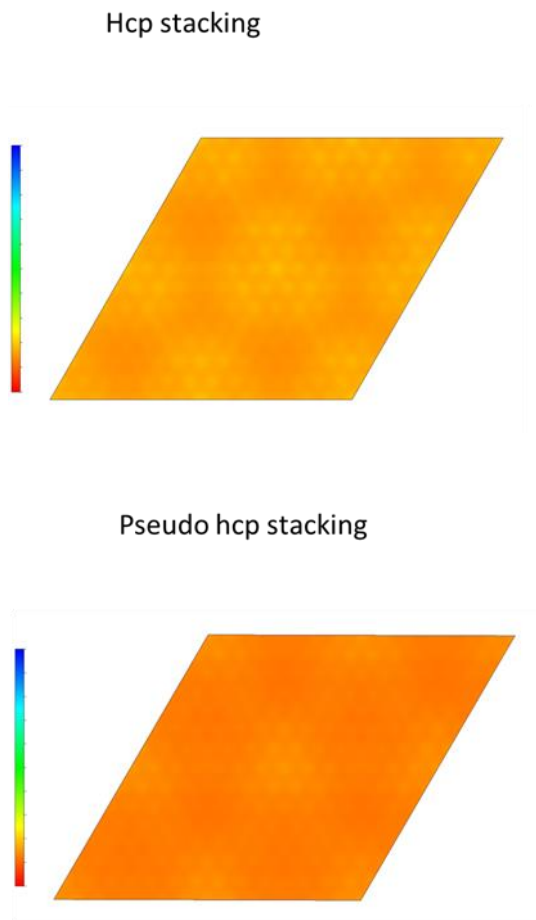


Figure 12. Calculations of the integrated local density of states (LDOS) for hcp structure Co slab model without stacking fault (Hcp stacking) and slab model with two stacking fault (Pseudo hcp stacking)

Magnetic thin films with perpendicular magnetic anisotropy (PMA) have attracted considerable attention in the last decade from the viewpoint of technological applications such as high density magnetic storage, magnetic random access memory, and other spintronics applications. Cobalt (Co) is a typical material for experimental studies of PMA in magnetic nanoscale structures because it has several advantageous properties: strong uniaxial magnetic anisotropy and the ability to control its properties in various shapes such as single atoms, nanoscale islands, and thin films. In particular, nanosized Co clusters or islands are attractive for ultrahigh-density magnetic-recording applications and, therefore, it is important to identify and characterize factors that may be detrimental to such applications. One of the factors that drastically reduce the magnetic anisotropy is stacking faults in intrinsic hcp structures. However, we are not thus far aware of any experimental efforts to investigate the effects microscopically at an atomically controlled level.

In this study, we performed microscopic investigations of the electronic and magnetic properties of Co nanoscale islands on a Ag(111) substrate by using a combination of spin-polarized scanning tunneling microscopy (SPSTM) experiments and density functional theory (DFT) calculations.

Cobalt islands with triangular or hexagonal shapes and thicknesses ranging from five to eight monolayers (MLs) were grown on the substrate. The islands were found to exhibit a moiré pattern. The islands were categorized into two groups with respect to the corrugation amplitude of the pattern in STM topographic images taken at -0.2 V as islands with stronger and weaker moiré-corrugation amplitudes. Via nanoscale magnetometry based on SPSTM, we found that the islands with stronger

moiré corrugation exhibit hysteretic magnetization curves with perpendicular magnetizations while the ones with weaker moiré corrugation exhibit in-plane magnetization without hysteresis. By calculating the magnetic anisotropies of the islands, we figured out that the magnetocrystalline anisotropy of the Co nanoislands, which favors perpendicular magnetization, is significantly reduced due to the presence of an fcc stacking fault in an intrinsic hcp structure. Upon increasing the number of stacking faults to two, the magnetocrystalline anisotropy becomes weaker than the shape anisotropy of the islands, which favors in-plane magnetization, thus resulting in a variation in the easy-magnetization axis from perpendicular to in-plane. Calculations of the integrated local density of states (LDOS) reproduced the observed moiré contrasts, which indicate that the difference in the moiré corrugation amplitude arises from the difference in the stacking structure; the pure hcp and the structures with a single fcc stacking fault, or the ones with more than two stacking faults. This result strongly suggests that the effect of an fcc stacking fault on the intrinsic hcp structure plays an important role in determining the electronic and magnetic properties of the Co nanoscale structures.

(6) Surface phonon excitation on clean metal surfaces in scanning tunneling microscopy [*Phys. Rev. B*, **93**, 085411 (2016)]

Inelastic electron tunneling spectroscopy (IETS) carried out with scanning tunneling microscopy (STM) provides a way of obtaining the vibrational fingerprint of a single molecule on a solid surface. The knowledge accumulated by the STM-IETS experiments enables us to control the vibration-induced chemical reactions by STM at the level of a single molecule. In STM-IETS, a tunneling electron from the STM tip excites molecular vibrations via the energy transfer through the

electron-phonon coupling (EPC) whenever the energy of tunneling electron exceeds the vibrational energies. This opens up an inelastic channel in parallel with the elastic one, giving rise to an increase/decrease of the differential conductivity dI/dV where I is the tunneling current and V the voltage applied to the STM junction. Because of the extremely small change in dI/dV with respect to that of elastic one, it is common to measure the second derivative of the tunneling current, d^2I/dV^2 , which is referred to the IETS spectrum. The symmetry of the electron and hole tunneling makes the IETS spectrum anti-symmetric with respect to the Fermi level. As a consequence, the IETS spectrum of a single molecule shows peak-dip pairs at the bias voltages corresponding to the molecular vibrations. In terms of the excitation of localized molecular vibration characterized by a discrete energy spectrum, the theory of the STM-IETS spectrum has been established, and the peak position in the spectrum is well interpreted by the vibrational density of states (DOS) of the molecule.

Until recently, the application of STM-IETS was limited to the localized vibration of single atoms and molecules adsorbed on surfaces. In principle, STM-IETS should be capable of detecting the collective lattice dynamics, i.e., phonons. Indeed, the STM-IETS measurement has been demonstrated on highly ordered pyrolytic graphite (HOPG), Au(111) and Cu(111), as well as the Pb island on Cu(111). Contrary to the STM-IETS of a single molecule with discrete vibrational levels, it is an open question how we analyze the STM-IETS spectra of solid surfaces with a continuous dispersion of phonon energies. Though the peak position in the IETS spectrum of HOPG is explained by a singular feature in the intensity of the phonon DOS derived from the flat dispersion, such a straightforward assignment is not valid for the cases of Au(111) and Cu(111). Very recently, it has been pointed out that the STM-IETS spectrum for a Pb islands on Cu(111) is described by

the Eliashberg function that consists of the product of energy-dependent EPC and phonon DOS (M. Schackert et al., Phys. Rev. Lett. 114, 047002 (2015)). The previous report, however, lacks the solid theoretical formulation that is required to connect the Eliashberg function to the inelastic tunneling current.

In this study, we first measured the STM-IETS spectrum on Cu(110). In the IETS spectrum measured at a Cu(110) clean surface, a peak-dip pair appears at ± 6 mV. Similar to the case of Au(111) and Cu(111), this spectrum cannot be rationalized by the phonon DOS either. In order to respond to the necessity for a theoretical formulation of STM-IETS that is applicable to phonon excitations in solids, we formulated the inelastic tunneling current and the STM-IETS spectrum using the non-equilibrium Keldysh Green's function technique.

The Hamiltonian of a system including the interactions between the STM tip, substrate conduction electrons and phonons in the substrate can be written as

$$H = \sum_p \varepsilon_p c_p^\dagger c_p + \sum_{k,\eta} \varepsilon_k^\eta c_{k\eta}^\dagger c_{k\eta} + \sum_{q,\lambda} \hbar\omega_q^\lambda a_{q\lambda}^\dagger a_{q\lambda} + \sum_{p,k,\eta} W_{pk}^\eta (c_p^\dagger c_{k\eta} + h.c.) + \sum_{k,p,\lambda,\eta,\eta'} M_{kp}^{\eta'\eta\lambda} c_{k+q\eta'}^\dagger c_{k\eta} (a_{q\lambda} + a_{-q\lambda}^\dagger), \quad (2)$$

where p , λ and η are the indices of the eigenstate of the tip, phonons and band of conduction electrons, respectively. k and q is the wave vector of the conduction electron and phonon, respectively. c_p , $c_{k\eta}$ and $a_{q\lambda}$ are the annihilation operators for electrons in the tip state, conduction electrons and substrate phonons whose energies are ε_p , ε_k^η and $\hbar\omega_q^\lambda$, respectively. W_{pk}^η is the substrate-tip tunneling matrix element, whereas $M_{kp}^{\eta'\eta\lambda}$ is the

EPC matrix element.

By the definition of the Keldysh Green's function $G_{ij}^{-+}(t, t') = i \langle c_j^\dagger(t') c_i(t) \rangle$, the stationary tunneling current can be written as,

$$I = -\frac{4e}{\hbar} \Re \int d\omega \sum_{pk\eta} W_{kp}^\eta W_{pk}^\eta \left(G_{pp}^{0r}(\omega) G_{k\eta k\eta}^{-+}(\omega) + G_{pp}^{0-+}(\omega) G_{k\eta k\eta}^a(\omega) \right), \quad (3)$$

where \Re stands for the real part.

If ρ_p (density of the states at the tip) and W_{pk}^η are constant with respect to the bias voltage, we obtain the following formula of the STM-IETS spectrum by taking the second derivative of $f(\omega - eV)$ with respect to the bias voltage and performing partial integral with respect to ω .

$$\frac{d^2 I}{dV^2} = -\frac{8\pi e^3}{\hbar} \sum_{pk\eta} |W_{pk}^\eta|^2 \rho_p \left| \frac{\partial}{\partial \omega} \Im G_{k\eta k\eta}^r(\omega) \right|_{\omega=eV}. \quad (4)$$

With in the second order of the EPC, the $d^2 I/dV^2$ can be approximated as

$$\frac{d^2 I}{dV^2} \propto \sum_{\lambda\eta\eta'} |M_{\Gamma\Gamma}^{\eta'\eta\lambda}|^2 \delta(E_F - \varepsilon_\Gamma^\eta)^2 \delta(E_F - \varepsilon_\Gamma^{\eta'}) \times \{ \delta(eV - \omega_\Gamma^\lambda) - \delta(-eV - \omega_\Gamma^\lambda) \} \quad (5)$$

The final formula of STM-IETS (eq. (5)) resembles the formula of the Eliashberg function $\alpha^2 F(\omega)$ which is defined as

$$\alpha^2 F(\omega) = \frac{1}{2\pi\rho(E_F)} \sum_{k,q,\lambda,\eta,\eta'} \frac{2\pi}{\hbar} |M_{k-q}^{\eta'\eta\lambda}|^2 \times \delta(E_F - \varepsilon_k^\eta) \delta(E_F - \varepsilon_{k-q}^{\eta'}) \delta(\omega - \omega_{\lambda q}) \quad (6)$$

Here $\rho(E_F)$ is the DOS of the conduction electron at the Fermi level. The Eliashberg function is the integration of the product of the energy dependent EPC (α) and phonon DOS ($F(\omega)$). Thus, we conclude that the STM-IETS signal on a metal surface is proportional to the momentum-resolved Eliashberg function,

$$\alpha^2 F(\omega, k = q = 0) = \sum_{\lambda\eta\eta'} |M_{\Gamma\Gamma}^{\eta'\eta\lambda}|^2 \times \delta(E_F - \varepsilon_\Gamma^\eta) \delta(E_F - \varepsilon_\Gamma^{\eta'}) \delta(eV - \omega_\Gamma^\lambda) \quad (7).$$

We evaluate the central term of the momentum-resolved Eliashberg function $M_{\Gamma\Gamma}^{\eta'\eta\lambda}$ by the ab-initio calculation based on DFPT. Within the DFPT scheme, $M_{\Gamma\Gamma}^{\eta'\eta\lambda}$ is defined as

$$M_{\Gamma\Gamma}^{\eta'\eta\lambda} = \sqrt{\frac{\hbar}{2M\omega_q^\lambda}} \langle \Gamma, \eta' | \left| \frac{\delta V_{scf}(r)}{\delta R_q^\lambda} \right| \Gamma, \eta \rangle, \quad (8)$$

with M being the mass of the atom. $|\Gamma, \eta\rangle$ is the Kohn-Sham state of conduction electron with the band index η at $\bar{\Gamma}$. $V_{scf}(r)$ is the self-consistent Kohn-Sham potential and $\frac{\delta V_{scf}(r)}{\delta R_q^\lambda}$ corresponds to the first-order correction to the potential due to the atomic displacement R_q^λ associated with the phonon mode λ with the wave vector q .

Ab-initio calculations for electron and phonon states as well as momentum-resolved Eliashberg function were performed at the level of the generalized gradient approximation (GGA) with the Perdew-Burke-Ernzerhof (PBE) functional by using QUANTUM-ESPRESSO. We modeled the surface with a 21-layer Cu(110) slab with a ~ 20 Å thick vacuum along the surface normal. The atoms in the slab were fully relaxed without any constraint until the forces on individual atoms were less than 5.0×10^{-4} a.u. An ultrasoft pseudopotential generated with the Rappe, Rabe, Kaxiras, and Joannopoulos (RRKJ3) scheme is used for Cu. The expansion of the plane-wave basis set is restricted by a kinetic energy cut-off of 35 Ry. For the phonon calculations, we set the charge density cut-off to 400 Ry. A $12 \times 12 \times 1$ Monkhorst-Pack grid without an offset is used for the ionic relaxation and self-consistent electronic structure calculations. The phonon DOS, dispersion and the EPC were calculated by density functional perturbation theory (DFPT) on the uniform $3 \times 3 \times 1$ grid in the surface Brillouin zone, which includes the high symmetry points. The phonon dispersion obtained by these settings is consistent with the previous study.

Figure 13 shows the calculated results of $\alpha^2 F(\omega, k = q = 0)$, which corresponds to the positive-bias side of the IETS spectrum. The single peak at 4 meV coincides with the peak structure in the IETS spectrum. This peak structure originates from the out-of-plane polarized phonon mode whose displacement is mainly distributed in the 1st and 2nd Cu layers. Such a phonon mode has never been detected in the previous experiments by helium atom scattering. The reason why this phonon mode selectively has strong EPC can be explained by the selection rule deduced from the symmetry consideration at the $\bar{\Gamma}$ point.

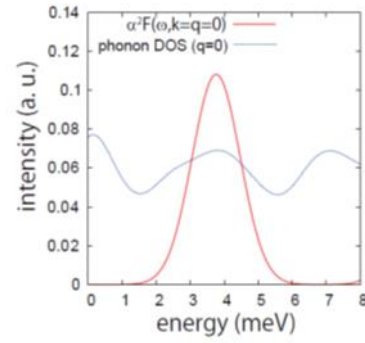


Figure 13. Calculation result of the momentum-resolved Eliashberg function on Cu(110)

(7) Surface carrier dynamics in energy conversion processes [*Nanotechnology* **26**, 365402 (2015)]

Dynamics of energetic carriers in semiconductors has attracted much attention from both fundamental and technological viewpoint. In particular, scattering, recombination and diffusion at semiconductor surfaces are the key processes that determines the operational efficiency of (opto)electronic devices and (photo)catalytic systems. The recent development of various nano-materials further raises the importance to precisely understand carrier dynamics at surfaces because such materials have large surface-to-volume ratios. Recently, surface carrier

dynamics in the electroluminescence processes can be investigated with atomic spatial resolution by using STM-induced light emission (STM-LE), where luminescence is induced by the tunneling current of STM (Figure 14). Atomically-resolved mapping of photoemission intensities provides unprecedented information that cannot be obtained by any other optical techniques.

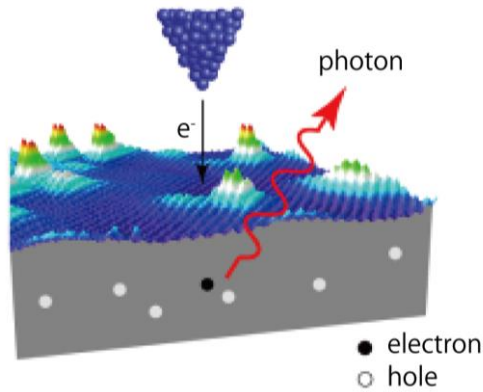


Figure 14. Schematic of STM-induced light emission from p-type GaAs. Luminescence is induced by electron injection from an STM tip.

In this financial year, combining theoretical and experimental analyses, we investigated the dynamics of energetic electrons at a (110) surface of GaAs that is one of the most important industrial materials used in optoelectronic devices. Since the presence of surface states in GaAs(110) would strongly affect the behavior of electrons, a detailed investigation of the electronic structure and electron dynamics at surfaces reveal unprecedented phenomena that have never been recognized in the study of carrier dynamics in the bulk material. We have studied these points by means of STM-LE experiments as well as DFT calculation and an effective model calculation.

DFT calculations were performed at the level of local density approximation (LDA) implemented in VASP code. Seventeen atomic (110) planes were used to model the surface system with a vacuum region of

more than 15 Å, where bottom atoms were terminated with hydrogen. A $12 \times 16 \times 1$ I^* -centered k-point grid was used for Brillouin zone sampling.

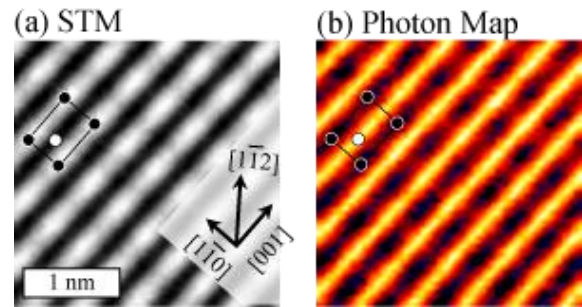


Figure 15. (a) An atomically resolved STM image and (b) an STL photon map of GaAs(110) acquired at the sample bias voltage $V_s = 1.8$ V. A unit cell at identical positions is shown (black: Ga, white: As).

Figure 15 (a) shows the STM image of a GaAs (110) surface. The atomic row appears along the [001] direction. This indicates the presence of surface states contributing to electron tunneling from the STM tip to the sample. Figure 15 (b) shows the photon map, where photon emission was induced by the tunneling current and the photon intensity was measured with varying the position of STM tip. Step-like patterns also appear to run along the [001] direction. However, in contrast to the STM image which shows bright spots near the surface states, dark spots were observed near the surface states in the photon map.

To reveal the mechanism for local variation in the photon intensity, we investigate the electronic structure of GaAs (110) surface using DFT calculations. Figure 16 (a) shows the band structure of the GaAs(110) surface and the projected bulk band structure. The first unoccupied surface band (C3 band) has valleys at the I^* and X -points of the surface Brillouin zone. Although the bottoms of these valleys are located at almost identical energy levels, the C3 band is resonant with the bulk CB at I^* point,

and it lies within the energy gap of the projected bulk band at the X -point. Because other valleys in the C3 band and the upper unoccupied surface bands are located higher in energy, tunneling electrons would be dominantly injected into the Γ and X -valleys of the C3 band, when the sample voltage is slightly above the band gap.

Figures 16 (b)-(d) show spatial distribution of charge densities ($|\Psi_{\Gamma}|^2$ and $|\Psi_{X}|^2$) of the electronic states in the C3 band at Γ and X -points, respectively. Figure 16 (b) clearly indicates that $|\Psi_{\Gamma}|^2$ penetrates into the bulk, whereas $|\Psi_{X}|^2$ is localized at the surface. Figure 16 (c) indicates that $|\Psi_{\Gamma}|^2$ distributes uniformly on the surface. In contrast, $|\Psi_{X}|^2$ is localized around the surface Ga atoms (Figure 16 (d)). Based on these results, it is concluded that when the STM tip is positioned above the surface Ga atoms, the surface states near the X -point mainly contributes to the electron tunneling, and that when the tip is above the center of the unit cell, surface states near the Γ -point dominantly contribute to the electron tunneling.

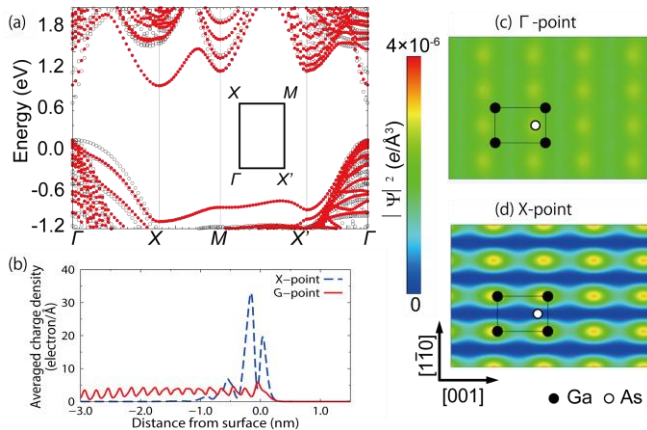


Figure 16. (a) Band structure for GaAs(110) surface (red closed circle) and projected bulk band structure (black open circle). Inset shows the surface Brillouin zone. (b) Charge densities integrated in planes parallel to the surface were plotted as a function of the distance from the surface. (c), (d) Charge densities in a (110) plane at 4 Å above the surface As atom.

As a next step, we considered the dynamics of the electrons injected into the surface states using a rate equation approach. We constructed the effective model, where the electron tunneling from the electronic states of the STM tip to the surface states, radiative and non-radiative recombination in the surface states, and intervalley scattering between the surface states at Γ and X -points were described. The photoemission rate I_{ph} was formulated as,

$$I_{\text{ph}}(\mathbf{r}, V) = Y \frac{(1-Q)(1-Pk(\mathbf{r}, V)) I_t}{1-Q(1-P)} \frac{1}{e},$$

where \mathbf{r} is the position of the tip and V is the sample voltage. Y is the internal quantum efficiency of the luminescence in the bulk, Q is the probability of electron scattering from Γ to X -point, P is the probability of non-radiative surface recombination, k is the ratio of the tunnelling current injected into the surface states near X -point to the total tunneling current I_t , and e is the elementary charge. The calculation results were compared with the rate estimated from the experimental results, where the ratio of I_{ph} with the tip position above the surface Ga atom and above the centre of the unit cell is about 54%. Based on our experimental and theoretical investigation, it is found that the probability P of non-radiative recombination at the surface is more than 46%. This high probability strongly suggests that the electron injected from the STM tip dissipate its energy mainly by the processes of non-radiative recombination through the surface states. This is suggestive of the fast scattering of injected electrons into the surface states.

In summary, we have unveiled the energy dissipation mechanism of electrons at the GaAs(110) surface based on atomically resolved STM-LE observations and theoretical analysis. Tunneling electrons injected into the surface mainly undergo non-radiative recombination through the surface states localized near the surface Ga atoms. The present study provides novel insight into the carrier

injection, scattering and recombination processes in electroluminescence of semiconductors. The microscopic analysis of these processes would contribute to the fundamental understanding of carrier dynamics in optoelectronic conversion processes and aid in the design of novel materials for optoelectronic devices.

4. Conclusion

We have tried to examine a variety of molecular behaviors on the surface in FY2015. Our theoretical studies combined with experiments in FY2015 provide deep insight into a variety of chemical and physical phenomena on solid surface. We expect that our results can provide new perspective to develop a potential strategy for controlling electronic properties of molecular adsorbates on the surface.

5. Schedule and prospect for the future

(1) Controlling chemical reactivity of ultrathin oxide film

Ultrathin oxide film grown on metal substrate has been a subject of great interest not only as a supporting material for chemically active nanoparticles but also as a catalyst in the field of heterogeneous catalysis, where it provides various ways to control the properties of adsorbates via following factors: (i) charge transfer between adsorbates and oxide-metal interface, which is closely correlated with the electronic affinity (EA) of adsorbate and workfunction reduction, (ii) adhesion between oxide and metal layers with strong polaronic distortion, (iii) film thickness, and (iv) the chemical composition of oxide surface.

Therefore, we will continue our work to find the way for controlling the chemical reactivity using

theoretical and experimental studies. In FY2016, we will extend our study into dissociation of CH_3OH and O_2 on $\text{MgO}/\text{Ag}(100)$ using combined STM and DFT methodology. In particular, regarding the CH_3OH dissociation on $\text{MgO}/\text{Ag}(100)$, we will try to find a way to selectively dissociate a bond in CH_3OH , e.g., C-H, O-H, and C-O, using an ionic species on MgO film surface which is introduced through charge transfer between the oxide surface and oxide-metal interface. For the O_2 dissociation on $\text{MgO}/\text{Ag}(100)$, we should consider an influence from the charge redistribution between the oxide-metal interface and the adsorbate, because of O_2 has much higher EA than that of H_2O molecule. The other branch of our study is clear understanding of the drawing effect at the oxide-metal interface, which can enhance the concentration of dopants at the interface. In addition, we have interests in other ultrathin oxide film systems, such as titania and ceria. We believe that our study provides not only profound insight into the chemical reactivity control of ultrathin oxide film but also an impetus for investigating ultrathin oxide films for a wider range of applications.

(2) Molecular adsorption on solid surface: From single molecule to molecular network

The controllable fabrication of molecular architectures is a topic of great importance not only as a fundamental subject in surface science but also for realizing molecular-scale electronic devices. Computational techniques can provide the underlying mechanisms for the formation of various molecular architectures experimentally observed by STM as well as single molecule adsorption. For the adsorption of single molecules on metal substrate, we suggested the origin of adsorption-induced stability reversal of photochromic DAE on metal surfaces and revealed that the interfacial orbital interaction originated from the weak electronic coupling between the molecular π -state and the

electronic states of the Au surface can play a decisive role in constraining adsorption geometry even in the archetypal vdW adsorption system. For one-dimensional (1-D) systems, we have explained (i) the formation mechanism of 1D zipper-type architecture of azobenzene derivatives with the balanced non-bonding interactions, H-bonding and vdW interactions, between adjacent molecules and (ii) the dispersive electronic feature due to the π -orbitals stacking in 1-D molecular lines fabricated on the Si(001)-(2 \times 1)-H. For 2D systems, we contributed to unveil the adsorption geometry of 2D molecular films composed of fluorinated fullerene (C₆₀F₃₆), which is strongly related to the distribution of frontier molecular orbitals and thus the n-type character of molecular film. In addition, we recently revealed the novel formation mechanism of supramolecular assembly using photochromic diarylethene derivative, which is the first report on molecular architectures formed by ion-dipole interaction on solid surface. Our results provide not only deeper insight into the molecular adsorption process, but also a general basis for designing the architectures of molecular electronics with desired electronic properties. In FY2016, we will continue the research not only for a variety of molecular assemblies but also isolated molecule on the surfaces as follows: (1) 2-D DNBA molecular assembly and (2) the formation mechanism of van der Waals interface between π -conjugated molecule and novel metal substrate.

(3) Electronic structures of functionalized graphene grown on metal substrate

Functionalization of graphene has attracted great scientific interest not only in controlling the physical properties of graphene, such as opening band gap to achieve semiconducting nature, but also in improving chemical adaptability to integrate graphene as a building block into a variety of

functional devices. In particular, we first suggested that the atomic oxidation of graphene grown on a metal substrate results in the formation of graphene enolate, i.e., negatively charged oxygen adsorbed at ontop position on its basal plane, which is strikingly different from the formation of epoxy groups, i.e., adsorption of atomic oxygen at bridge position, on pristine graphene and on graphite. Whereas the enolate is the transition state between two nearest epoxides both on graphene and on graphite, we revealed that improved interfacial interaction between graphene and metal substrate during atomic oxidation plays a crucial role not only in the formation of graphene enolate as a local minimum but also in stabilizing it over the graphene epoxide. In FY2016, we are going to theoretically investigate our very recent experimental finding of well-ordered graphene functionalization, in which the formation of graphene enolate would be one of the main driving forces. Our results are expected to provide not only a novel perspective for a chemical route to functionalize graphene but also a new opportunity for graphene-based applications.

(4) Surface magnetism: spin-orbit interaction and its application toward ultra-high dense magnetic storage

From FY2016, we extend our research on surface magnetism toward the spin-orbit related phenomena. In FY2015, we found that the magnetic anisotropy energy is strongly affected by the stacking fault in thin film. This means that the control of the nanostructure at surface is one of the important key to realize the high efficient nonvolatile magnetic memories.

As prospect for the future, we plan to investigate the spin-orbit interaction and resulting magnetic anisotropy in (1) single molecule on surface (2) single magnetic atom on oxide surface. Especially, we try to

find out the suitable combination of molecule/atom and surface to realize high magnetic anisotropy energy and controllability with the external electric field. To achieve this goal, we carry out high-throughput ab-initio calculations for rapid materials screening.

(5) Photoelectric conversion in single molecule on surface

Our studies on carrier dynamics in energy conversion processes are extended to the research on photoelectric conversion in single molecule. Luminescence from a single molecule can be induced by the tunneling current of STM. This enables us to investigate the electroluminescence processes of a molecule with submolecular spatial resolution in a well-defined manner. Especially, we focus on electron correlations in electroluminescence processes, e.g., charging of the molecule, formation of single/triplet excitons, radiative and nonradiative decay, and so forth. The key factor in the theoretical analysis is the calculation of (i) excited electronic states of the molecule with a high efficiency and accuracy as well as (ii) nonequilibrium electron dynamics in electroluminescence processes under applied bias. We plan to investigate these points using the method based on first-principles many-body perturbation theory (MBPT) and the nonequilibrium Green's function (NEGF) methods. Our study would make a contribution for understanding the fundamental nature of molecular electroluminescence and in the designing of novel functional materials for organic (opto)electronic devices.

Fiscal Year 2015 List of Publications Resulting from the Use of the supercomputer

* The members registered as the user of RICC system in FY2015 are indicated by underline.

[Publication]

1. K. Doi, E. Minamitani, S. Yamamoto, R. Arafune, Y. Yoshida, S. Watanabe, Y. Hasegawa, “Electronic and magnetic effects of a stacking fault in cobalt nanoscale islands on the Ag (111) surface”, *Phys. Rev. B*, **92** (6), 064421 (Aug. 2015).
2. E. Minamitani, Y. Fu, Q.-K. Xue, Y. Kim, S. Watanabe, “Spatially extended underscreened Kondo state from collective molecular spin”, *Phys. Rev. B*, **92** (7), 075144 (Aug. 2015).
3. E. Minamitani, R. Arafune, N. Tsukahara, Y. Ohda, S. Watanabe, M. Kawai, H. Ueba, and N. Takagi, “Surface phonon excitation on clean metal surfaces in scanning tunneling microscopy”, *Phys. Rev. B*, **93** (8), 085411 (Feb. 2016).
4. H. Imada, K. Miwa, J. Jung, T. K. Shimizu, N. Yamamoto, and Y. Kim, “Atomic-scale luminescence measurement and theoretical analysis unveiling electron energy dissipation at a p-type GaAs(110) surface”, *Nanotechnology*, **26** (36), 365402 (Aug. 2015).
5. K. Miwa, H. Imada, M. Sakaue, H. Kasai, and Y. Kim, “Nonequilibrium Green's Function Theory of Scanning Tunneling Microscope-Induced Light Emission from Molecule Covered Metal Surfaces: Effects of Coupling between Exciton and Plasmon Modes”, *e-J. Surf. Sci. Nanotech.*, **13**, 385 (Aug. 2015).
6. Z. Liang, H. J. Yang, J. Oh, J. Jung, Y. Kim, and M. Trenary, “Atomic-scale dynamics of surface-catalyzed hydrogenation/dehydrogenation: NH on Pt(111)” *ACS Nano*, **9** (8), 8303 (Jul. 2015).
7. E. Kazuma, M. Han, J. Jung, J. Oh, T. Seki, and Y. Kim, “Elucidation of isomerization pathways of a single azobenzene derivative using an STM”, *J. Phys. Chem. Lett.*, **6** (21), 4239 (Oct. 2015).
8. J.-H. Kim, J.-C. Ribierre, Y. S. Yang, C. Adachi, M. Kawai, J. Jung, T. Fukushima, and Y. Kim, “Seamless growth of a supramolecular carpet” *Nat. Commun.*, **7**, 10653 (Feb. 2016).
9. Y. H. Song, N. Singh, J. Jung, H. Kim, E.-H. Kim, H.-K. Cheong, Y. Kim, and K.-W. Chi, “Template-free synthesis of a molecular Solomon link by two-component self-assembly”, *Angew. Chem. Int. Ed.*, **55** (6), 2007 (Feb. 2016).

[Oral presentation at an international symposium]

1. K. Miwa, H. Imada, M. Sakaue, H. Kasai, and Y. Kim, “Quantum Interference between Exciton and Plasmon Dynamics in Scanning Tunneling Microscope-induced Light Emission”, The 9th International Symposium on Ultrafast Surface Dynamics (USD9), Shiga, Japan (May 2015).
2. E. Minamitani, “Nobel Kondo effects in single molecules on metal surfaces”, Studying the Function of Soft Molecular Systems by the Concerted Use of Theory and Experiment. The 12th Workshop: Theory, Measurement and Creation of Porphyrinoid Compounds as Soft Molecular Systems, Ibaraki, Japan (invited, October 2015).